Engineering Silver-Enriched Copper Core-Shell Electrocatalysts to Enhance the Production of Ethylene and C$_{2+}$ Chemicals from Carbon Dioxide at Low Cell Potentials

Andrew N. Kuhn, Haidong Zhao, Uzoma O. Nwabara, Xiaofei Lu, Mingyan Liu, Yung-Tin Pan, Wenjin Zhu, Paul J. A. Kenis,* and Hong Yang*

Copper catalysts are widely studied for the electroreduction of carbon dioxide (CO$_2$) to value-added hydrocarbon products. Controlling the surface composition of copper nanomaterials may provide the electronic and structural properties necessary for carbon-carbon coupling, thus increasing the Faradaic efficiency (FE) towards ethylene and other multi-carbon (C$_{2+}$) products. Synthesis and catalytic study of silver-coated copper nanoparticles (Cu@Ag NPs) for the reduction of CO$_2$ are presented. Bimetallic CuAg NPs are typically difficult to produce due to the bulk immiscibility between these two metals. Slow injection of the silver precursor, concentrations of organic capping agents, and gas environment proved critical to control the size and metal distribution of the Cu@Ag NPs. The optimized Cu@Ag electrocatalyst exhibited a very low onset cell potential of −2.25 V for ethylene formation, reaching a FE towards C$_{2+}$ products (FE$_{C_{2+}}$) of 43% at −2.50 V, which is 1.0 V lower than a reference Cu catalyst to reach a similar FE$_{C_{2+}}$. The high ethylene formation at low potentials is attributed to enhanced C−C coupling on the Ag enriched shell of the Cu@Ag electrocatalysts. This study offers a new catalyst design towards increasing the efficiency for the electroreduction of CO$_2$ to value-added chemicals.

1. Introduction

The development of useful applications for carbon dioxide (CO$_2$) is of great interest because of its increasing atmospheric concentration and its associated impact on global temperature.[1,2] Conversion of CO$_2$ to value-added chemicals remains challenging and has relied on the use of heterogeneous catalysts for improved reaction kinetics.[3–5] Thermal activation of a carbon-oxygen double bond often requires the use of costly reducing agents (e.g., hydrogen gas) and noble metal catalysts (e.g., Pd, Au), as well as energy-intensive post-separation processes.[6–9] Electrolysis holds promise for catalytic upgrading of CO$_2$ to generate valuable products especially when energy

comes from sustainable sources. Electrochemical processes can in principle also be employed at an industrially-relevant scale.[10–14] Precious metals such as gold (Au) and silver (Ag) are promising catalysts for CO$_2$ electroreduction.[7–9,14–17] These metals generally favor the formation of carbon monoxide (CO) with near 100% Faradaic efficiency (FE) over a broad range of operating potentials. In principle, subsequent electroreduction of CO could provide an indirect route to multi-carbon (C$_{2+}$) products from starting with CO$_2$, especially due to the increased surface CO species required for C−C coupling.[18–22] Significant efforts have been made to improve the electroreduction of CO by engineering new catalytic surfaces and identifying reaction pathways.[23–27] Much work is still required for this process to be useful for the direct conversion of CO$_2$ to valuable chemicals. The use of non-noble metals has also been studied recently to create active catalysts for the electroreduction of CO$_2$. For example, metals such as tin (Sn), zinc (Zn), and indium (In) were reported to catalyze the reduction of CO$_2$ to oxygen-containing C$_1$ products, including formate (HCOO$^-$) and CO.[28–35] However, techno-economic analyses suggest that reduction to yield liquid alcohols (e.g., methanol, ethanol, and propanol) and ethylene gas (C$_2$H$_4$) is likely required to make the process of CO$_2$ reduction economically viable.[36,37]

Copper is the best-known transition metal capable of forming the energy-dense C$_{2+}$ molecules, and a promising metal electrocatalyst for the direct upgrading of CO$_2$.[38–48] The FEs for alcohols, however, remain low at a low cell potential (<2.50 V), even though the FEs for C$_2$H$_4$ can be as high as 60% at high cell potentials (>3.00 V).[49,50] The products of C$_{2+}$ product from CO$_2$ on Cu catalysts are thought to undergo C−C coupling and that adsorbed CO* is the key intermediate.[22,49,51–54] DFT studies further suggest that the moderate binding energy of CO* on Cu facilitates the reduction to alcohols and hydrocarbons.[55,56] To improve the performance, material designs (e.g., tuning the nanoporosity and surface engineering) are common strategies.[57,58] One important solution to tune the electronic properties of Cu is to design bimetallic electrocatalysts that combine a noble metal with Cu (e.g., CuPd, CuAg, and CuAu).[49,59–70] CuAg

A. N. Kuhn, Prof. H. Zhao, U. O. Nwabara, Dr. X. Lu, M. Liu,
Prof. Y.-T. Pan, W. Zhu, Prof. P. J. A. Kenis, Prof. H. Yang
Department of Chemical and Biomolecular Engineering
University of Illinois at Urbana-Champaign
600 South Mathews Avenue, Urbana, IL 61801, USA
E-mail: kenis@illinois.edu; hy66@illinois.edu

**ADVANCED
SCIENCE NEWS**
www.advancedsciencenews.com

**ADVANCED
FUNCTIONAL
MATERIALS**
www.afm-journal.de

bimetallic catalysts are particularly important and reported to have increased conductivity, stability, and local concentration of surface carbon monoxide species (CO*).[15,16,36,43,65–68,70] Research on CuAg catalysts often relies on large nanoparticles (NPs, >30 nm), likely due to the challenges for making bimetallic NPs between two immiscible metals, highlighting the synthetic need and importance for controlling the atomic ratio and nanostructures between Cu and Ag towards generating active sites.[65–67,70] Strain effects of Ag atoms on the surface of CuAg nanocrystals may also promote multi-carbon products.[65] However, the FE to C_{2+} products at low cell potentials (−2.50 V) remains small (<5%) for the large Cu-based catalysts, but can reach to ≈45% when the cell potential is raised above −3.00 V. On another front, nanowire systems offer a structural benefit for their performance, owing to their high electrochemically-active surface areas and a large number of low-coordinated surface atoms at steps and edges.[38,68] Cu and CuAg nanowires (≈100 nm diameter) have been reported to achieve exceptionally high initial FEs towards C_{2+} products (≈80%) at low potentials (−2.50 to −3.00 V). However, rapid deactivation from structural rearrangement and loss of surface area under reaction conditions hinder the practical application of these nanowire catalysts.

In this work, we present an approach to engineering the surface and electronic structures of Cu nanocatalysts with the precision coatings of Ag to facilitate C−C coupling in the electroreduction of CO_2. We show although Cu and Ag are immiscible in bulk, solution-phase synthesis can lead to the formation of Ag coating on the surface of Cu NPs from sub-atomic monolayer to a few layers thick, creating Cu@Ag core-shell electrocatalysts. Furthermore, metallic Cu is active in various liquids and may readily oxidize during the synthesis.[71,72] To overcome these challenges, we used a solution-phase method for

producing spherical NPs with tunable sizes by controlling the capping ligands and reduction conditions as described in the literature.[64,73–77] With the proper control, a second metal might be deposited on the surface of the as-made NPs.[64,71–74] Optimization of the synthesis conditions for the second step nevertheless requires careful design in order to obtain core-shell NPs of desired structure and composition. Herein, we present a solution-phase synthesis for the growth of an Ag coating on sub-10 nm Cu nanoparticles (Cu@Ag NPs). Addition rate of silver precursor, type and concentration of organic capping agents, and composition of the gas environment proved critical to obtaining the Cu@Ag NP catalysts with small sizes and narrow size distributions. The average thickness of the Ag-enriched shell could be as small as 0.1 nm, likely a partial Ag monolayer that may also bond with Cu atoms detectable by surface-sensitive characterization techniques. The Cu@Ag catalyst had a low onset potential (−2.25 V) for the electroreduction of CO_2 to C_2H_4 and achieved a FE of 43% towards C_{2+} products at −2.50 V which was triple that of a reference Cu nanoparticle catalyst. The high FE at low potentials was attributed to enhanced C−C coupling from an increased concentration of surface CO* species on the Cu@Ag catalysts and offers a new approach towards increasing the overall efficiency of the cell for the electroreduction of CO_2 to multi-carbon products.

2. Results and Discussion

2.1. Formation of Cu@Ag Nanoparticles

The synthesis used in these experiments was modified from multiple sources.[64,73,74,77,78] **Figure 1**a highlights the key synthesis
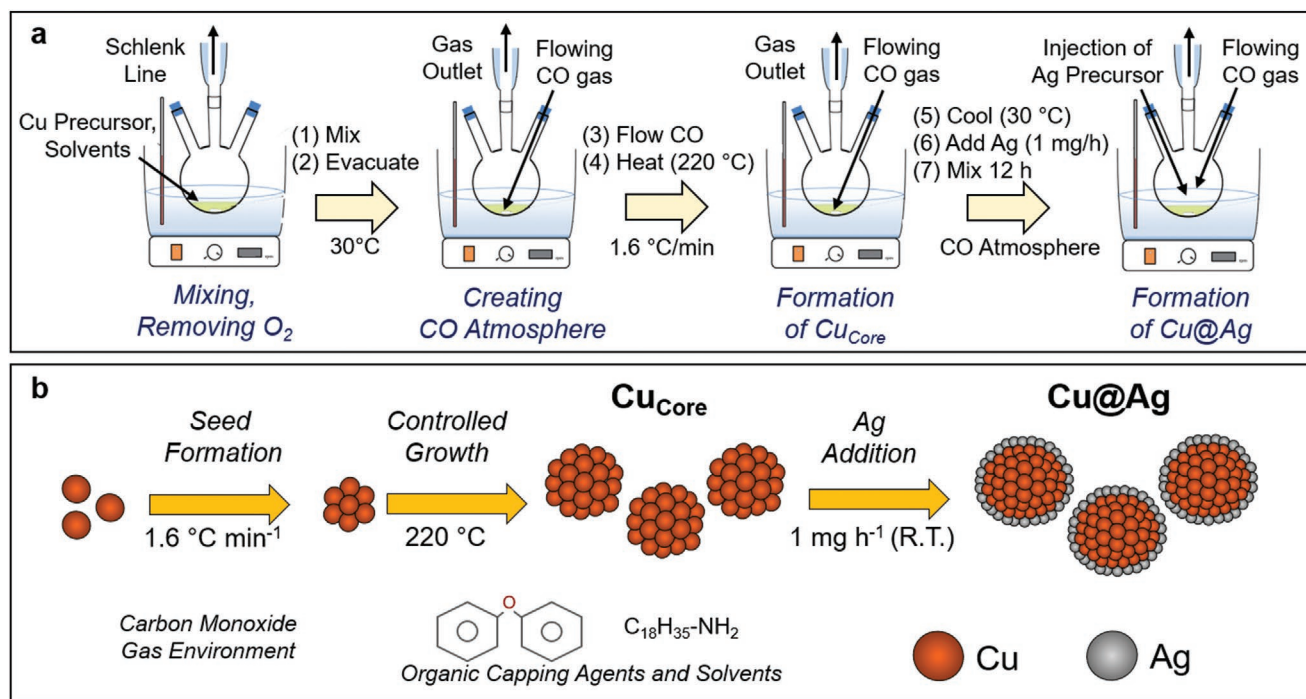

Figure 1. a) Scheme for the synthesis of Cu@Ag core-shell nanoparticle electrocatalysts and b) the illustration of the formation of Cu@Ag NPs.
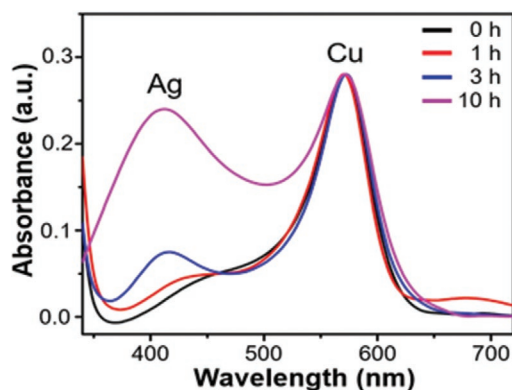
Figure 2. UV–vis curves revealing the presence and growth of the Ag-enriched shell as a function of injection time. The curves were normalized to the height of the Cu peak.

steps and features, including the gas environment, solvent and capping agents, and temperature profile throughout the process. The starting Cu solution contained $Cu(acac)_2$, oleylamine (OAm), and diphenyl ether (DPE). A Schlenk line was used to evacuate the flask and to introduce CO gas. The temperature was slowly ramped to 220 °C (1.6 °C min^{-1}) and held for 2 h. The vessel was then cooled to 30 °C. A portion of the NPs, labeled as Cu_{Core}, was taken at this point for characterization. For the formation of Cu@Ag NPs, a solution of $AgOCOCF_3$ dissolved in OAm was slowly injected (1 mg Ag h^{-1}) to the Cu_{Core} suspension at 30 °C while CO was flowing. The injection lasted 10 h and the mixture was stirred for an additional 12 h to ensure uniform growth of the Ag-enriched shell.[69,70] The Cu_{Core} and Cu@Ag NPs were collected by centrifugation, washed with hexane and methanol, and dispersed in hexane for further use. Figure 1b is a proposed atomic scheme for the formation of the Cu@Ag NPs through the process outlined in Figure 1a. **Figure 2** analyzes the ultraviolet-visible (UV–vis) absorption spectra of the Cu@Ag NPs after different durations of time for the addition of silver using the characteristic UV–vis peaks for Cu (580 nm) and Ag (410 nm). The Ag peak, which was initially absent, appeared after the reaction for 3 h, and significantly increased after 10 h. This observation suggests an increase in the thickness of the Ag-enriched shell during the reaction process. Transmission electron microscopic (TEM) images show the particles uniformly grew from the 6.5 nm Cu_{Core} NPs (**Figure 3**a) to form Cu@Ag

NPs with a size of 6.8 nm after 1 h (Figure 3b), to 7.6 nm after 3 h (Figure 3c), and to 8.4 nm after 10 h (Figure 3d). The size distribution was relatively constant during this process with a standard deviation around 0.8 nm, thus Ag atoms were added nearly uniformly on the surface of the Cu_{Core} NPs. The growth in particle sizes observed in TEM after 3 h (Figure 3c) to 10 h (Figure 3d) agrees with the large increase in the Ag peak of the UV–vis spectra (Figure 2).

The concentration of DPE proved important towards the particle size and size distribution of the Cu_{Core} NPs. Figure S1 a–c, Supporting Information, shows the TEM micrographs of Cu core nanoparticles formed under different DPE concentrations: 9.3 ± 1.6 nm without DPE, 6.5 ± 0.7 nm using 60 µM DPE, and 6.4 ± 0.6 nm using 120 µM DPE. We observed that further increasing the amount of DPE above 120 µM had no significant impact on the size of Cu NPs since the concentration of Cu in the solution was 430 mM, which was three orders of magnitude more than that of DPE. This result suggests that the presence of DPE slowed down the growth of the Cu_{Core} NPs and ensured a narrow particle size distribution. Similarly, DPE affected the particle sizes and size distributions of Cu@Ag NPs: 10.6 ± 1.6 nm without DPE, 8.4 ± 0.7 nm using 60 µM DPE, and 6.7 ± 0.6 nm using 120 µM DPE (Figure S1 d–f, Supporting Information). Note that the change of particle size from the Cu_{Core} to the Cu@Ag NPs was only 0.3 nm when 120 µM of DPE was used. Considering the spherical nature of these particles, the shell thickness should be approximately half of this value, which was about ≈0.15 nm. This sample was named $Cu@Ag_{0.1nm}$. Since the radius of Ag atom is larger than 0.15 nm, the result indicates the Ag-enriched shell should be less than one monolayer thick. In other words, the surface is rich in Ag but exists as a bimetallic mixture between Cu and Ag. When no DPE was used in the synthesis, the particle had a ≈0.3 nm thick Ag-enriched shell ($Cu@Ag_{0.3nm}$). The surface Ag atoms in $Cu@Ag_{0.3nm}$ are strained and electronically distinctive from a pure Ag NP. The injection rate of the silver precursor solution, the gas environment, and the choice of surfactant also affected the particle size and size distribution (Figure S2, Supporting Information). Fast addition of $AgOCOCF_3$ solution caused the particles to grow at different rates thus significantly increasing the particle size and size distribution of the NPs from 6.4 ± 0.6 nm to 8.3 ± 3.6 nm. Using argon (Ar) in the synthesis resulted in the formation of large Cu@Ag particles (9.7 ± 2.8 nm), while using oleic acid (OAc) instead of DPE
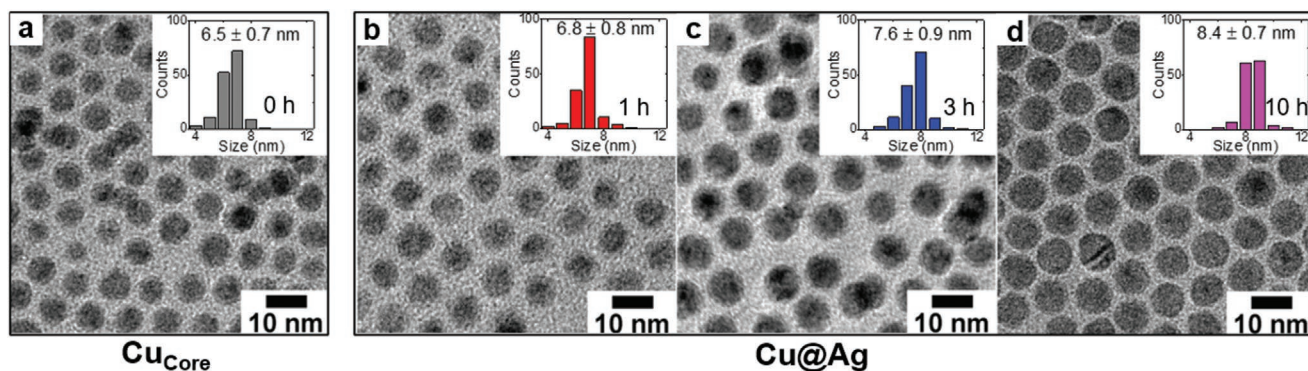

Figure 3. TEM images and size distribution of a) the Cu_{Core} and Cu@Ag NPs after b) 1, c) 3, and d) 10 h of Ag injection.

Table 1. Synthesis parameters and the resulting particle size of Cu and Cu@Ag NPs.

| Sample Type	Rate of Ag Injection [mg h⁻¹]	Gas	DPE [μM]	OAc [μM]	Particle Size [nm]
Cu_Core	N/A	CO	0	0	9.3 ± 1.9
			60	0	6.5 ± 0.7
			120	0	6.4 ± 0.6
Cu@Ag	1.0	CO	0	0	10.0 ± 1.6
			60	0	8.4 ± 0.7
			120	0	6.7 ± 0.6
Control Cu@Ag	1.0	CO	0	120	Aggregated
	2.0	CO	120	0	8.3 ± 3.6
	1.0	Ar	120	0	9.7 ± 2.8

Figure 4. Representative XRD patterns for a) Cu_Core and b) Cu@Ag NPs. JCPDS patterns: 04–0783 (Ag, green), 03-065-9026 (Cu, red), and 05–0667 (Cu₂O, blue).

caused aggregation of the NPs. These results agree with the previous studies on the synthesis of NPs in organic solutions and highlight the effects of reducing and capping agents on the stabilization of NPs in OAm-rich solvents.[64,73,77] Note that temperature selection during the synthesis also played a critical role, but that is not the focus of this work. Slow ramping rates of heat are necessary to ensure a narrow particle size distribution. Overheating above the temperature for Cu_Core NP formation (here 220 °C) causes aggregation and the formation of non-spherical particles. The addition of the Ag precursor at 30 °C allowed for kinetic control of the thickness while maintaining a high yield. The impact of the aforementioned synthesis features speaks to the sensitivity of the Cu@Ag NP system which allows for some tunability but also highlights the potential challenges with reproducibility and scale-up. **Table 1** summarizes the effect of critical synthesis parameters on the size and size distribution of Cu_Core and Cu@Ag NPs obtained in this study.

2.2. Evaluation of the Cu@Ag Structures

X-ray diffraction (XRD) was used to identify the crystalline phases and provide information on the compositional properties of the Cu_Core and Cu@Ag catalysts made from mixtures using 60 μM of DPE (**Figure 4**). The XRD pattern of the Cu_Core in Figure 4a contains sharp peaks for metallic Cu and broad peaks for cuprous oxide (Cu₂O). The Cu NPs likely oxidized upon removal of the capping agent and exposure to air. For the Cu@Ag sample, we used the NPs with a shell thickness of around 0.9 nm to facilitate the identification of the Ag-rich shell by XRD (Figure 4b). The face-centered cubic (fcc) phase of pure Cu and Ag metals could be indexed, and the broad peaks were due to the small particle size. The (111) diffraction peaks of Ag at 38° 2θ appeared to have a slight shift in the Cu@Ag sample, indicated by the orange arrow. The XRD study suggests there exists a close interaction between Cu and Ag in the Cu@Ag NPs. While Cu and Ag do not readily mix in the bulk phase, the formation of mixed CuAg can occur in nanostructures.[38,61] No Cu₂O peaks were detectable because the Ag-rich shell protected the Cu core from oxidation when exposed to air.

Figure 5 contains characterizations to elucidate the structural and compositional features of the surface of the Cu@Ag NPs.
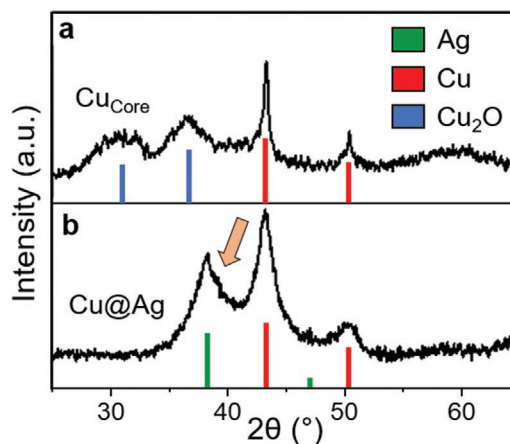
The high-resolution TEM (HRTEM) image shows the Ag-enriched shell and Cu core, judging by the differences in contrast (Figure 5a). This sample was made with 60 μM DPE which yielded a shell thickness of around 1 nm, allowing the easier microscopic detection of the core-shell-like structures. HRTEM study shows the (111) lattice fringes of the Cu@Ag NP having an average spacing of 0.215 nm (Figure 5b). Since the typical lattice spacings are 0.209 nm for pure fcc Cu (111) and 0.236 nm for pure Ag (111), the observed value indicates the Ag-enriched shell contained Cu based on Vegard's law. Such effects have been known to affect the structure and catalytic activity of bimetallic NPs.[79] Figure 5c shows the scanning transmission electron microscopy (STEM) dark field image and the corresponding elemental mapping of the Cu@Ag NPs. All of the particles show the Cu signal dominant in the central regions with Ag localized around the edges, though Cu could still exist in the shell. The composition of these NPs was measured to be approximately Cu₈₂Ag₁₈ by energy dispersive spectroscopy (EDS, Figure S3, Supporting Information). If we assume the Cu_Core was 7 nm, this atomic ratio of Cu to Ag would imply an approximate 7.5 nm Cu@Ag NP (0.25 nm thick Ag-rich shell) which is consistent with the values from Table 1. The surface chemical features of Cu@Ag NPs were analyzed based on X-ray photoelectron spectroscopy (XPS) survey scan (Figure 5d), Cu 2p (Figure 5e), and Ag 3d regions (Figure 5f). Both Cu and Ag were observed because the depth of the XPS beam is a few nanometers. The Cu atoms have a mixed valency with the majority being metallic Cu (red), and the remainder being Cu¹⁺ (blue), as shown in Figure 5e. Although the Cu@Ag did not contain oxidized Cu peaks in the XRD which analyzes the whole particle (Figure 4b), the surface Cu atoms appeared partially oxidized as seen by the XPS spectra. The Ag 3d pattern (Figure 5f) shows that silver is metallic. Overall, the XPS data further confirms the formation of Cu@Ag bimetallic NP catalysts.

2.3. Performance for the Electroreduction of CO₂

The as-synthesized Cu_Core, Cu@Ag₀.₁ₙₘ, and Cu@Ag₀.₃ₙₘ NPs were supported onto carbon with a mass loading of 20 wt.%

**ADVANCED
SCIENCE NEWS**
www.advancedsciencenews.com

**ADVANCED
FUNCTIONAL
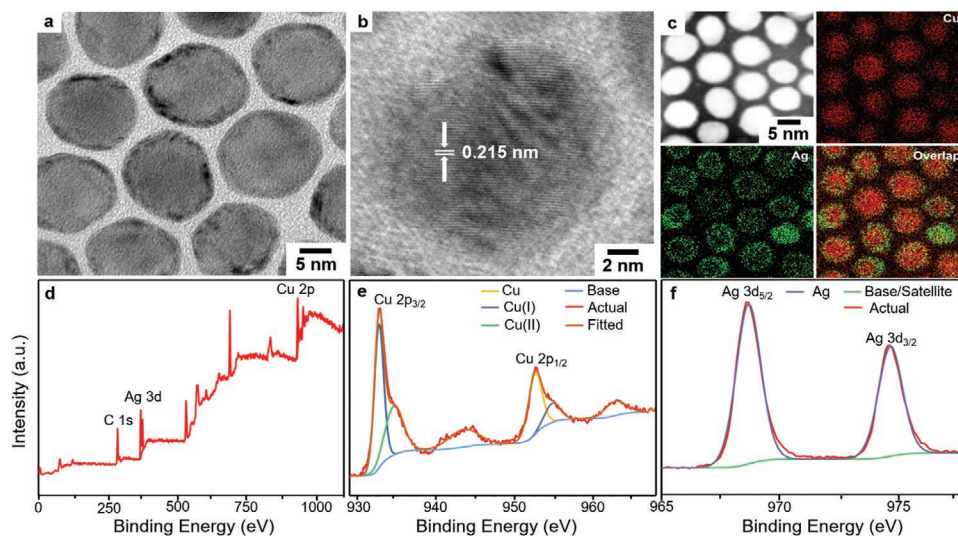MATERIALS**
www.afm-journal.de

Figure 5. Characterizations to elucidate the structures and compositions of the Cu@Ag NPs. HRTEM image showing the a) Ag-enriched shell and Cu core through contrast differences and b) the lattice spacing of strained Ag-enriched shell. c) STEM elemental mapping of Cu (red) and Ag (green). XPS of d) survey scan, e) Cu 2p, and f) Ag 3d regions.

(by total metal) as described in the Experimental Section. The final materials were examined for their electrocatalytic reduction of CO_2 gas using a flow cell setup. The corresponding cathode potential for each cell potential is provided in Table S1, Supporting Information, for all catalysts tested. The current densities are statistically similar for all catalysts at each cell potential (Figure S4, Supporting Information). Notably, the total current density was around 60 mA cm^{-2} at −2.25 V and around 110 mA cm^{-2} at −2.50 V. **Figure 6** shows the FEs for all of the measurable carbon products at the set cell potentials for Cu@Ag$_{0.1nm}$, Cu@Ag$_{0.3nm}$, and the two reference catalysts

made of Cu (Cu$_{Ref.}$) and Ag (Ag$_{Ref.}$).[38] The bar diagrams in Figure 6 are color-coded based on the type of products: C_{2+} products are a shade of red, CO is gray, and the other C_1 products are a shade of blue. At cell potentials between −1.75 and −2.00 V, the catalysts that contain Cu exclusively produced oxygenated products: CO, formate, and acetate (Figure 6a–c). Although acetate (H_3CCOO^-) is a C_2 product, its high oxygen content makes it the least desirable of the multi-carbon products.[37] When the potential was increased to −2.25 V, marked with a single asterisk (*), the formation of ethylene (dark red) switched on for the Cu@Ag$_{0.1nm}$ electrocatalyst with a FE$_{C2H4}$
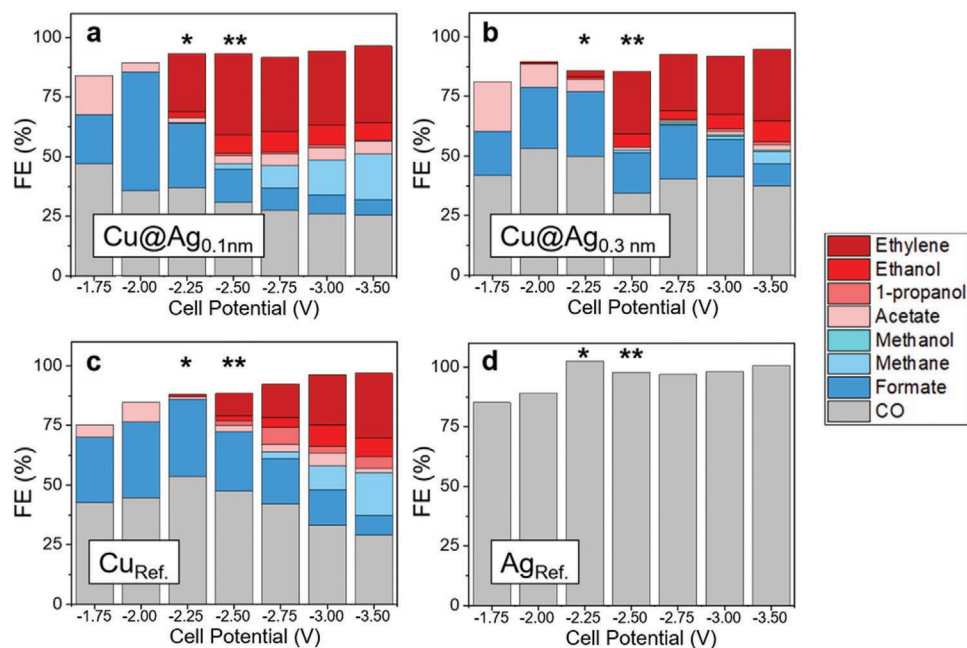

Figure 6. FE for carbon products as a function of cell potential in the electroreduction of CO_2 using an in-line setup: a) Cu@Ag$_{0.1nm}$, b) Cu@Ag$_{0.3nm}$, c) reference Cu, and d) reference Ag.

of 27% (Figure 6a). This value was five times greater than that of Cu@Ag$_{0.3nm}$ (Figure 6b) and ten times greater than that of Cu$_{Ref.}$ (Figure 6c) at this cell potential. The total FE increased for all four electrocatalysts as the potential was raised, reaching between 90 and 100% for each sample. Table S2, Supporting Information, contains the FE to H$_2$ gas at all potentials for the tested catalysts. Generally, H$_2$ forms via the hydrogen evolution reaction at high cell potentials. In the region of interest (−2.25 to −2.75 V), the gas chromatograph (GC) peaks for H$_2$ were too low to be quantified properly.

Generally speaking, the individual FEs of C$_{2+}$ products (namely ethylene, ethanol, and 1-propanol) were maximized at the highest tested cell potential (−3.50 V) for the three Cu-containing catalysts because of the high energy barrier for these molecules. However, the highest FE for C$_{2+}$ products (43%) was achieved for the Cu@Ag$_{0.1nm}$ electrocatalyst at −2.50 V, marked with a double asterisk (**) in Figure 6a. Although the Cu@Ag$_{0.1nm}$ electrocatalyst had a comparable value at −3.50 V (FE of 42%), operating at the lower cell potential (−2.50 V) is preferred because of the higher energy efficiency and the lower FE towards methane (CH$_4$). The latter reason is kinetically relevant because the formation of CH$_4$ often indicates that adsorbed carbon species (C$_1$*) are directly reduced without C−C coupling, representing an undesired pathway that prevents the formation of C$_{2+}$ products.[80] The FE of CH$_4$ was only 2% for Cu@Ag$_{0.1nm}$ at −2.50 V, suggesting that C−C coupling was faster than the reduction of C$_1$* species to CH$_4$ at this condition. Additionally, the reduction of adsorbed two-carbon species (C$_2$*) had a preferred pathway to form C$_2$H$_4$ (34% FE) than the formation of oxygen-containing C$_{2+}$ products. Acetate, ethanol, and 1-propanol had a combined 9% FE at −2.50 V. In contrast, the Cu$_{Ref.}$ catalyst had a FE of only 14% towards C$_{2+}$ products at −2.50 V and required a cell potential of −3.50 to reach a value of 41%. Therefore, Cu@Ag$_{0.1nm}$ requires 1.0 V less in cell potential to reach >40% FE to C$_{2+}$ products in comparison to a traditional copper catalyst. Ag$_{Ref.}$ selectively produced CO with a high FE (Figure 6d) which suggests that Ag atoms in the Cu@Ag catalysts may activate the first C=O double bond in CO$_2$ which initiates the pathway for C$_{2+}$ products.[15,16,65] The contributions of surface strain and Cu-Ag alloying may also play a role in the high selectivity towards C$_{2+}$ products at low cell potentials. The FEs of the Cu$_{Core}$ were similar to those of Cu$_{Ref.}$ (Figure S5, Supporting Information). C$_2$H$_4$ first appears at −2.50 V (16% FE$_{C2H4}$) and the FE$_{C2+}$ was maximized at 39% at −3.50 V.

In **Figure 7**, we highlight the FE towards C$_{2+}$ products (FE$_{C2+}$) and ethylene (FE$_{C2H4}$) for the Cu@Ag and Cu$_{Ref.}$ electrocatalysts at the intermediate potentials (−2.25 to −2.75 V). The FE$_{C2+}$ at −2.50 V was 43% for Cu@Ag$_{0.1nm}$, 32% for Cu@Ag$_{0.3nm}$, and 14% for Cu$_{Ref.}$ (Figure 7a). This result proves that there is a substantial benefit to the Ag-enriched shell for C−C coupling at low cell potentials. More than 80% of the C$_{2+}$ products that were formed from Cu@Ag samples was C$_2$H$_4$ at −2.50 V. In contrast, only 70% of the C$_{2+}$ products were C$_2$H$_4$ for Cu$_{Ref.}$, suggesting that the mechanistic pathways of C−C coupling favor ethylene formation at −2.50 V for Cu@Ag$_{0.1nm}$ (34% FE$_{C2H4}$) and Cu@Ag$_{0.3nm}$ (26% FE$_{C2H4}$) as compared to Cu$_{Ref.}$ (8% FE$_{C2H4}$). Figure S6, Supporting Information, compares the FE$_{C2+}$ and FE$_{C2H4}$ of Cu$_{Core}$ with Cu$_{Ref.}$ at the potentials of −2.25, −2.50, and −2.75 V. The Cu$_{Core}$ had a higher FE$_{C2H4}$ and comparable
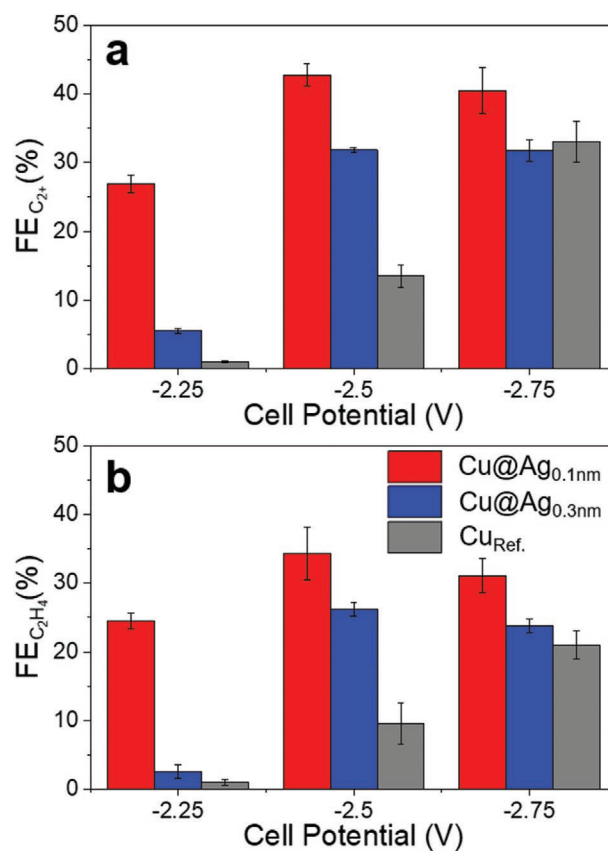

Figure 7. Faradaic efficiencies to a) C$_{2+}$ products and b) ethylene during the electro-reduction of CO$_2$ at medium cell potentials for Cu@Ag and Cu$_{Ref.}$ catalysts.

FE$_{C2+}$ in this region. Notably, the C$_{2+}$ products from the Cu$_{Core}$ were dominated by C$_2$H$_4$ (96%) at −2.50 V, agreeing with the general observation. Energy Dispersive X-ray Fluorescence (EDXRF) was used to analyze the stability of copper-silver atomic ratio in Cu@Ag$_{0.1nm}$ after the electrochemical CO$_2$ testing (Figures S7 and S8, Supporting Information). The fresh powder was Cu$_{82}$Ag$_{18}$, whereas the catalyst deposited on the electrode was Cu$_{93}$Ag$_7$ after the reaction. These values approach the error associated with the technique and the different sample types. We hypothesize that the latter value (Cu$_{93}$Ag$_7$) may be more representative of the stabilized core-shell composition. Additionally, this result suggests that the Cu core was preserved by the Ag-rich coating.

Tables S3,S4, Supporting Information, compare the performance of the Cu@Ag electrocatalysts with the recently reported CuAg bimetallic catalysts for the electroreduction of CO$_2$. For this comparison, we converted the cell potentials into cathode potentials based on the 1.0 M KOH electrolyte used in this work. The cell potential of −2.50 V is equal to −0.75 V versus RHE at the cathode and −3.00 V becomes −1.10 V versus RHE. All other nanoparticle systems fail to reach FEs for C$_2$H$_4$ and C$_{2+}$ products above 3% at −0.75 V versus RHE (Table S6, Supporting Information). The Cu@Ag$_{0.1nm}$ catalyst has a tenfold increase in FE$_{C2H4}$ and FE$_{C2+}$ at these conditions. It is important to note that the Cu@Ag NPs in this work are significantly smaller than the other catalysts in Tables S3,S4, Supporting Information.

ADVANCED
SCIENCE NEWS
www.advancedsciencenews.com

ADVANCED
FUNCTIONAL
MATERIALS
www.afm-journal.de

At a cathode potential of −1.10 V versus RHE (Table S3, Supporting Information), the performances of the Cu@Ag catalysts are similar to the literature values for CuAg: $FE_{C_2H_4}$ are 30–40% and $FE_{C_{2+}}$ are 40–50%. Based on the findings of this work and published mechanistic studies, we conclude that the controlled formation of an Ag-enrichment on the surface of sub-10 nm Cu NPs is a main contributor towards the higher $FE_{C_{2+}}$ at lower cell potentials. **Figure 8** is a summary scheme for the performance of the catalysts for the electro-reduction of CO_2 to C_{2+} products at a low cell potential (−2.50 V). The $FE_{C_{2+}}$ are 43% for Cu@Ag$_{0.1nm}$, 32% for Cu@Ag$_{0.3nm}$, 14% for Cu$_{Ref.}$, and 0% for Ag$_{Ref.}$. Based on this study and recent reports, our hypothesis is that the addition of silver atoms onto the surface of sub-10 nm copper nanoparticles favors carbon-carbon coupling at low potentials from strain effects, electronic tuning at the Cu-Ag interface, and increased concentration of adsorbed CO*. Mechanistic studies, through experiments and calculations, can be used to further our understanding of the structure-property relationship of our Cu@Ag catalytic system.

3. Conclusion

The size and structure of Ag-enriched Cu@Ag nanoparticles were kinetically controlled using a sequential synthesis of care-fully screened reactants, solvents, and reaction conditions. Stringent control over the addition of silver precursors under the heated carbon monoxide gas environment is important to obtain an Ag-enriched shell at a single or sub-mono- atomic layer accuracy. Using these well-controlled Cu@Ag catalysts, the electroreduction of CO_2 to ethylene was switched on at a low cell potential of −2.25 V and achieved a FE towards C_{2+} products of 43% at −2.50 V, of that >80% was C_2H_4. These results provide a new CO_2 reduction electrocatalyst based on fine structural control of two immiscible metals and the insights towards enhancing C−C coupling for the electroreduction of carbon dioxide through engineering the surface of bimetallic nanoparticle catalysts.

4. Experimental Section

Materials: Butylamine (99%), dimethyl sulfoxide (DMSO, ≥99.9%), DPE (99%), OAm (70%), oleic acid (OAc, 90%), tetrahydrofuran (THF, ≥99.0%), copper acetylacetonate (Cu[acac]$_2$, 99.99%), silver trifluoroacetate (AgOCOCF$_3$, 98%), reference silver electrocatalyst (Ag$_{Ref.}$, <100 nm, 99.5%), and potassium hydroxide (KOH, ≥85%) were purchased from Sigma-Aldrich. Deuterated water (D$_2$O), hexane, isopropanol (IPA), and methanol (ACS Standard Grades) were purchased from Fisher Chemical. Nafion (5 wt.%) solution was from Fuel Cell Earth. Ketjen black carbon with a specific area of 800 m^2 g$^{−1}$
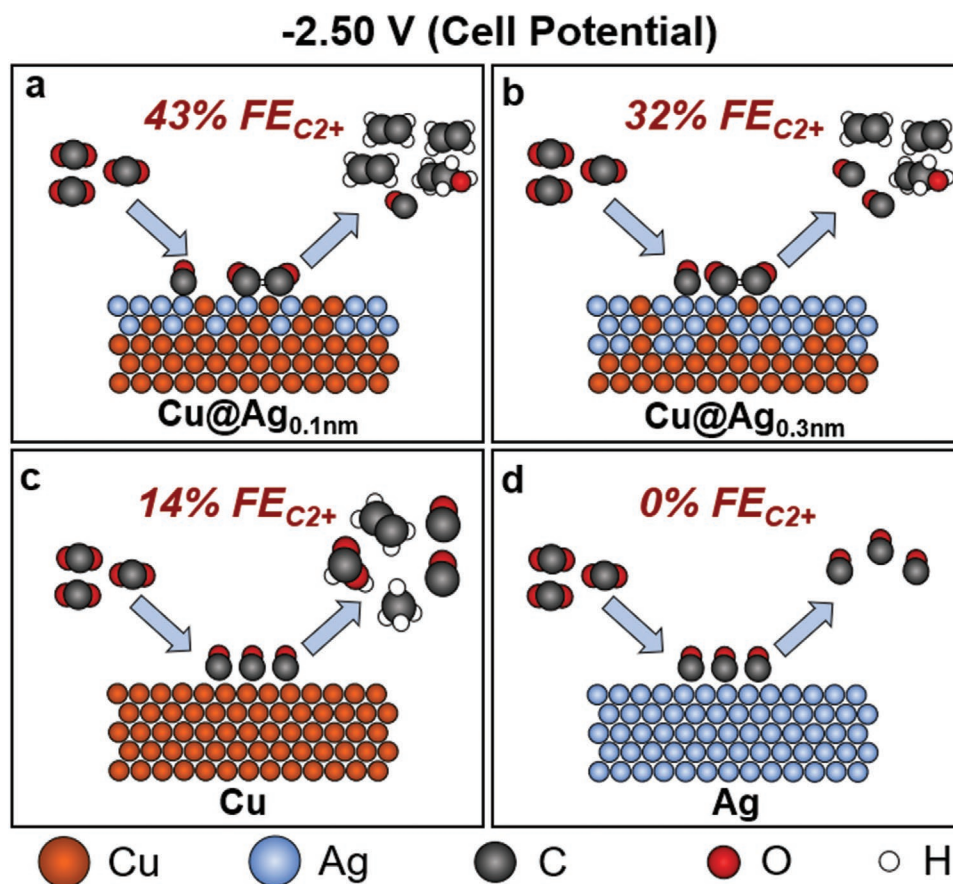

Figure 8. Schematic illustration summarizing the FE of C_{2+} products for the electroreduction of CO_2 by various electrocatalysts at a low potential: a) Cu@Ag$_{0.1nm}$, b) Cu@Ag$_{0.3nm}$, c) Cu, and d) Ag electrocatalysts.

ADVANCED
SCIENCE NEWS
www.advancedsciencenews.com

ADVANCED
FUNCTIONAL
MATERIALS
www.afm-journal.de

was used as the carbon support. Iridium oxide (IrO_2, non-hydrate) was purchased from Alfa Aesar. The reference Cu catalyst ($Cu_{Ref.}$) was made in lab and reported previously.[38] Argon (Ar, ultra-high purity), carbon dioxide (CO_2), carbon monoxide (CO), helium (He), hydrogen (H_2), and nitrogen (N_2) were purchased from Airgas Inc all at ultra-high purity grades. All chemicals and gases were used as received unless indicated otherwise.

Preparation of Cu Nanoparticles (Cu_{Core}): The synthesis of NPs used in these experiments was modified from multiple sources.[64,73,74,77,78] The growth of the Cu NPs was achieved in a single pot under a CO gas environment. The details of the original designs were reported elsewhere.[64,74] The schematic for the typical synthesis is provided in Figure 1a. In a standard procedure, Cu(acac)$_2$ (16 mg) was dissolved in OAm (9 mL) in a three-neck flask. DPE was added at a concentration of 120 µM. The resulting turquoise-blue solution was placed in an oil bath at 30 °C and continuously stirred during the following steps. A Schlenk line was purged using Ar gas and applied vacuum with a vacuum pump (Edwards, RV12). Before switching to Ar, the line was held under vacuum for 5 min to remove oxygen gas from the system. This process was repeated six times. Carbon monoxide gas was then introduced at a flow rate of 90 sccm. Caution: CO gas is toxic and should be handled with extra care in a well-vented chemical hood equipped with a CO detector. The temperature was maintained at 30 °C for 30 min, followed by being heated at a ramp rate of 1.6 °C min^{-1} to 220 °C using an oil bath. The color of the solution changed from transparent blue-green to yellow to reddish-brown during heating. The temperature of the vessel was kept at 220 °C for 2 h to ensure the completion of the reaction. Afterwards, the vessel was removed from the oil bath, allowed to cool naturally in about 1.5 h, and then placed in a second oil bath at 30 °C, all while flowing CO. A portion of the NPs, labeled as Cu_{Core}, was taken at this point for characterization. The effects of the concentration of DPE on the formation of Cu_{Core} NPs were tested at 0, 60, and 120 µM, respectively, while keeping all other conditions the same.

Preparation of Ag-Coated Cu Nanoparticles: An AgOCOCF$_3$ solution was prepared by adding a predetermined amount to OAm (2 mg mL^{-1}) in a 10 mL vial. The vial was sonicated for 30 min to ensure the salt was completely dissolved. A syringe pump (Chemyx Inc., F100) was used to inject 5 mL of the AgOCOCF$_3$ solution into the three-neck flask that contained the suspension of Cu_{Core} at 30 °C while CO was flowing (the final step shown in Figure 1a). The infusion rate of the Ag precursor solution was set at 0.5 mL h^{-1} (1 mg Ag h^{-1}) to ensure uniform growth of the Ag-enriched shell.[81,82] After 5 mL of the Ag precursor solution was added (10 mg added in 10 h), the mixture was stirred for an additional 12 h while maintaining the temperature at 30 °C and a flowrate of CO gas at 90 sccm. The formed NPs were collected by centrifugation (Beckman Coulter Model X-30) at 5000 rpm for 10 min, followed by washing with hexane as the dispersing agent (3 mL) and methanol as the antisolvent (17 mL). The particles, labeled as Cu@Ag, were dispersed in hexane for further use.

The effect of the concentration of DPE on the particle size and thickness of the Ag-enriched shell was studied at three concentrations: 0, 60, and 120 µM, respectively, like in the case of the Cu_{Core} samples. A sample at a faster infusion rate of the Ag precursor solution of 1 mL h^{-1} was prepared to study the effect of rate on the particle size distribution and thickness of the Ag-enriched shell. The total amount of Ag added to the Cu_{Core} suspension was constant at 10 mg, thus the injection time was decreased to 5 h. All other reaction conditions were kept the same. The role of the gas environment towards the structures of the Cu@Ag NPs was investigated by replacing CO with Ar gas (90 sccm), while using the standard synthesis conditions described above (120 µM of DPE and an infusion rate of the Ag precursor solution of 0.5 mL h^{-1}). As a control experiment, OAc (120 µM) was used instead of DPE to examine the effects of the organic surfactant on the formation of Cu@Ag particles. All other variables were kept constant during the synthesis.

Materials Characterization: Ultraviolet-visible absorption spectroscopy (UV–vis) was conducted using a Shimadzu UV-3600 spectrophotometer. Aliquots of the formed Cu@Ag NP suspensions were taken during the addition of Ag at pre-set times (0, 1, 3, and 10 h) and diluted using

hexane. The spectra were normalized using the highest peak centered around 580 nm. TEM was carried out at an acceleration voltage of 200 kV (JEOL 2100 Cryo), while STEM used 300 kV on an FEI Themis Z Advanced Probe Aberration Corrected Analytical STEM. High-angle annular dark-field (HAADF) was used for the elemental mapping by EDS. The specimens were prepared by dispersing the NPs in hexane, depositing the suspension onto a carbon-coated gold grid, and drying at 40 °C. The crystal structures (prior to loading onto carbon) were analyzed by powder XRD (Rigaku MiniFlex 600, equipped with a Photon 100 detector and a Cu X-ray source). The measurement was performed in transmission mode between 20 and 80° 2θ at a rate of 0.02° 2θ s^{-1}. XPS was performed on a Kratos Axis ULTRA using an Al Kα X-ray source. The samples were loaded on fluorine-doped tin oxide glass substrates and taped onto an XPS holder with Cu tape for measurements. The CasaXPS software was used for processing the data and fitting the peaks. EDXRF was performed on a Shimadzu EDX-700 spectrometer with Rh X-ray source. The Cu@Ag$_{0.1nm}$ sample was loaded in a sample cup with the bottom covered by polypropylene film. The Cu@Ag$_{0.1nm}$ catalyst that was on an electrode after being tested for the CO_2 electroreduction was directly loaded on the sample holder for testing.

Preparation of the Electrocatalysts: The Cu@Ag NPs were loaded on Ketjen black carbon at a nominal mass loading of 20% of total metals. The mass concentration of the suspension in hexane was determined by thermogravimetric analysis (TGA, Model: Q50) to be approximately 1 mg metal mL^{-1}. Three sets of data were collected by TGA and the average value was used to ensure the accuracy. Next, 10 mg of Ketjen black carbon was added in hexane (0.5 mg C mL^{-1} hexane) and sonicated for 30 min. The Cu@Ag NP suspension (2 mg of the solid) was added dropwise in ≈5 min. The carbon suspension in hexane was continuously stirred during the addition of Cu@Ag NPs and kept on for an additional hour afterwards. The resulting suspension was sonicated for 1 h, and the solids were separated using centrifugation (5000 rpm, 10 min). The particles were then dissolved in butylamine (1 mL mg^{-1}) to remove the organic materials from the surface for electrocatalytic activation.[83,84] This suspension was continuously stirred for 72 h while covered. The solid product was removed from the butylamine solvent by centrifugation (5000 rpm, 10 min) and washed once using hexane. The final Cu@Ag/C electrocatalyst was obtained by drying in Ar gas at room temperature. This synthesis procedure of carbon-supported electrocatalyst was done for three samples: Cu_{Core} (120 µM DPE), Cu@Ag (120 µM DPE), and Cu@Ag (0 µM).

Preparation of the Electrodes: The cathode catalysts were deposited via hand-painting on a carbon gas diffusion layer (GDL, Sigracet 35BC, Fuel Cell Store). A carbon-supported Cu@Ag electrocatalyst (2 mg) was mixed with THF (200 µL), IPA (200 µL), and Nafion (5.2 µL) to prepare the ink. The concentration of Nafion was 10 wt.% in the catalyst layer. The mixture was then sonicated for 20 min. The ink was then hand-painted on the cathode at a loading of 1.0 mg cm^{-2}. This procedure was repeated for the Cu_{Core} and Cu@Ag (0 µM) electrocatalysts. The inks for $Cu_{Ref.}$ and Ag$_{Ref.}$ were prepared similarly with the exception that DI water was used instead of THF. The anode material, IrO_2, was deposited by spray-coating with a loading of 1.0 mg cm^{-2} as reported previously.[73]

Electrochemical Testing: The electroreduction of CO_2 was tested using an alkaline flow cell setup as discussed in previous reports.[38,53] Gaseous CO_2 was continuously supplied to the back of the cathode at a rate of 17 sccm using a mass flow controller. A syringe pump (Harvard Apparatus, PHD 2000) continuously fed 1 M KOH (pH = 13.54) at 0.5 mL min^{-1} as the catholyte and anolyte through two polyether ether ketone (PEEK) electrolyte chambers separated by an anion exchange membrane (PK-75, Fumatech).[85] The cell potential was varied from −1.75 to −3.50 V via potentiostat (Autolab PGSTAT-30) and the corresponding current density was continuously measured. Multimeters (MS8233D) hooked up to the flow cell were used to measure cathode and anode potentials against an Ag/AgCl reference electrode (Basi, RE-5B). For a typical procedure, the cell was first hooked up to the CO_2 feed, electrolyte pump, potentiostat, multimeters, and gas chromatograph (GC, Thermo Finnigan Trace GC). A cell potential of −1.75 V was applied for 200 s in order to equilibrate and stabilize the current. The GC program was

then started for the first injection and a liquid electrolyte sample was manually collected from the catholyte. The current, cathode potential, and anode potential were recorded at this time. There was a ≈1 min wait time between each injection. Therefore, the cell ran for almost 5 min until the GC collected three gaseous samples. After the GC finished analyzing all injections for a given cell potential (10 min in total), the cell potential was changed while continuing to flow CO_2 and the KOH electrolyte. Seven predetermined cell potentials were applied and tested sequentially (−1.75. −2.00, −2.25, −2.50, −2.75, −3.00, and −3.50 V).

Evaluation of Products and Faradaic Efficiencies: The compositions of gas products at each potential were measured using a GC. Helium gas was the reference and carrier gas for the thermal conductivity detector (TCD), N_2 gas was the makeup gas, and H_2 gas was used for the flame ionization detector (FID). The TCD was used to measure the gas concentrations of CO, H_2, and CO_2, whereas the FID measured the values for CH_4 and C_2H_4. Three injections were taken to minimize errors. Liquid products were collected from the catholyte effluent and tested using nuclear magnetic resonance (NMR) spectroscopy (Agilent VNS750NB) to determine their concentrations. Typically, 100 µL of the catholyte sample was mixed with 100 µL of DMSO standard solution and 400 µL of deuterated water (D_2O) in an NMR tube. The DMSO standard solution was made by diluting the store-bought DMSO with D_2O to obtain the final concentration (1.262 mM). The samples were analyzed using ^1H NMR equipped with solvent suppression. The spectra were integrated and compared against a DMSO standard to quantify the concentrations of the liquid products to obtain the FE to each product at different cell potentials. In addition to collecting three data points at each cell potential, samples were tested three times from synthesis to performance evaluation. Associated error bars are included where appropriate.

Supporting Information

Supporting Information is available from the Wiley Online Library or from the author.

Conflict of Interest

The authors declare no conflict of interest.

Data Availability Statement

The data that support the findings of this study are available from the corresponding author upon reasonable requests.

[1] P. J. A. Kenis, A. Dibenedetto, T. Zhang, *ChemPhysChem* **2017**, *18*, 3091.

[2] P. De Luna, C. Hahn, D. Higgins, S. A. Jaffer, T. F. Jaramillo, E. H. Sargent, *Science* **2019**, *364*, eaav3506.

[3] H.-R. M. Jhong, S. Ma, P. J. A. Kenis, *Curr. Opin. Chem. Eng.* **2013**, *2*, 191.

[4] S. Das, J. Pérez-Ramírez, J. Gong, N. Dewangan, K. Hidajat, B. C. Gates, S. Kawi, *Chem. Soc. Rev.* **2020**, *49*, 2937.

[5] X. Jiang, X. Nie, X. Guo, C. Song, J. G. Chen, *Chem. Rev.* **2020**, *120*, 7984.

[6] X. Lu, Y. Liu, Y. He, A. N. Kuhn, P.-C. Shih, C.-J. Sun, X. Wen, C. Shi, H. Yang, *ACS Appl. Mater. Interfaces* **2019**, *11*, 27717.

[7] H.-R. Jhong, C. E. Tornow, C. Kim, S. Verma, J. L. Oberst, P. S. Anderson, A. A. Gewirth, T. Fujigaya, N. Nakashima, P. J. A. Kenis, *ChemPhysChem* **2017**, *18*, 3274.

[8] S. Verma, Y. Hamasaki, C. Kim, W. Huang, S. Lu, H.-R. M. Jhong, A. A. Gewirth, T. Fujigaya, N. Nakashima, P. J. A. Kenis, *ACS Energy Lett.* **2018**, *3*, 193.

[9] S. Ringe, C. G. Morales-Guio, L. D. Chen, M. Fields, T. F. Jaramillo, C. Hahn, K. Chan, *Nat. Commun.* **2020**, *11*, 33.

[10] S. Verma, U. O. Nwabara, P. J. A. Kenis, *Nanocarbons for Energy Conversion: Supramolecular Approaches* (Ed: N Nakashima), Springer International Publishing, Cham **2019**, pp. 219–251.

[11] U. O. Nwabara, E. R. Cofell, S. Verma, E. Negro, P. J. A. Kenis, *ChemSusChem* **2020**, *13*, 855.

[12] S. Malkhandi, B. S. Yeo, *Curr. Opin. Chem. Eng.* **2019**, *26*, 112.

[13] D. T. Whipple, P. J. A. Kenis, *J. Phys. Chem. Lett.* **2010**, *1*, 3451.

[14] L. Hou, J. Yan, L. Takele, Y. Wang, X. Yan, Y. Gao, *Inorg. Chem. Front.* **2019**, *6*, 3363.

[15] S. Ma, J. Liu, K. Sasaki, S. M. Lyth, P. J. A. Kenis, *Energy Tech.* **2017**, *5*, 861.

[16] S. S. Bhargava, F. Proietto, D. Azmoodeh, E. R. Cofell, D. A. Henckel, S. Verma, C. J. Brooks, A. A. Gewirth, P. J. A. Kenis, *ChemElectroChem* **2020**, *7*, 2001.

[17] Y. Zhao, C. Wang, Y. Liu, D. R. MacFarlane, G. G. Wallace, *Adv. Energy Mater.* **2018**, *8*, 1801400.

[18] M. Jouny, G. S. Hutchings, F. Jiao, *Nat. Catal.* **2019**, *2*, 1062.

[19] L. Wang, S. A. Nitopi, E. Bertheussen, M. Orazov, C. G. Morales-Guio, X. Liu, D. C. Higgins, K. Chan, J. K. Nørskov, C. Hahn, T. F. Jaramillo, *ACS Catal.* **2018**, *8*, 7445.

[20] D. Raciti, C. Wang, *Nat. Catal.* **2018**, *1*, 741.

[21] Y. Wang, D. Raciti, C. Wang, *ACS Catal.* **2018**, *8*, 5657.

[22] D. Raciti, L. Cao, K. J. T. Livi, P. F. Rottmann, X. Tang, C. Li, Z. Hicks, K. H. Bowen, K. J. Hemker, T. Mueller, C. Wang, *ACS Catal.* **2017**, *7*, 4467.

[23] W. Luc, X. Fu, J. Shi, J.-J. Lv, M. Jouny, B. H. Ko, Y. Xu, Q. Tu, X. Hu, J. Wu, Q. Yue, L. Yuanyue, F. Jiao, Y. Kang, *Nat. Catal.* **2019**, *2*, 423.

[24] Y. Pang, J. Li, Z. Wang, C.-S. Tan, P.-L. Hsieh, T.-T. Zhuang, Z.-Q. Liang, C. Zou, X. Wang, P. De Luna, J. P. Edwards, Y. Xu, F. Li, C.-T. Dinh, M. Zhong, Y. Lou, D. Wu, L.-J. Chen, E. H. Sargent, D. Sinton, *Nat. Catal.* **2019**, *2*, 251.

[25] Y. Wang, Z. Wang, C.-T. Dinh, J. Li, A. Ozden, M. G. Kibria, A. Seifitokaldani, C.-S. Tan, C. M. Gabardo, M. Luo, H. Zhou, F. Li, Y. Lum, C. McCallum, Y. Xu, M. Liu, A. Proppe, A. Johnston,

P. Todorovic, T.-T. Zhuang, D. Sinton, S. O. Kelley, E. H. Sargent, *Nat. Catal.* **2020**, *3*, 98.

[26] M. Jouny, W. Luc, F. Jiao, *Nat. Catal.* **2018**, *1*, 748.

[27] J. Li, D. Wu, A. S. Malkani, X. Chang, M.-J. Cheng, B. Xu, Q. Lu, *Angew. Chem., Int. Ed.* **2020**, *59*, 4464.

[28] D. H. Won, H. Shin, J. Koh, J. Chung, H. S. Lee, H. Kim, S. I. Woo, *Angew. Chem., Int. Ed.* **2016**, *55*, 9297.

[29] D. L. T. Nguyen, M. S. Jee, D. H. Won, H.-S. Oh, B. K. Min, Y. J. Hwang, *Catal. Commun.* **2018**, *114*, 109.

[30] F. Lei, W. Liu, Y. Sun, J. Xu, K. Liu, L. Liang, T. Yao, B. Pan, S. Wei, Y. Xie, *Nat. Commun.* **2016**, *7*, 12697.

[31] X. Zheng, P. De Luna, F. P. G. de Arquer, B. Zhang, N. Becknell, M. B. Ross, Y. Li, M. N. Banis, Y. Li, M. Lui, O. Voznyy, C. T. Dinh, T. Zhuang, P. Stadler, Y. Cui, X. Du, P. yang, E. H. Sargent, *Joule* **2017**, *1*, 794.

[32] K. Liu, J. Wang, M. Shi, J. Yan, Q. Jiang, *Adv. Energy Mater.* **2019**, *9*, 1900276.

[33] G. Wen, D. U. Lee, B. Ren, F. M. Hassan, G. Jiang, Z. P. Cano, J. Gostick, E. Croiset, Z. Bai, L. Yang, Z. Chen, *Adv. Energy Mater.* **2018**, *8*, 1802427.

[34] F. Wei, T. Wang, X. Jiang, Y. Ai, A. Cui, J. Cui, J. Fu, J. Cheng, L. Lei, Y. Hou, S. Liu, *Adv. Funct. Mater.* **2020**, *30*, 2002092.

[35] P. Lu, X. Tan, H. Zhao, Q. Xiang, K. Liu, X. Zhao, X. Yin, X. Li, X. Hai, S. Xi, A. T. S. Wee, S. J. Pennycook, X. Yu, M. Yuan, J. Wu, G. Zhang, S. C. Smith, Z. Yin, *ACS Nano* **2021**, *15*, 5671.

[36] A. Gallo, J. L. Snider, D. Sokaras, D. Nordlund, T. Kroll, H. Ogasawara, L. Kovarik, M. S. Duyar, T. F. Jaramillo, *Appl. Catal. B* **2020**, *267*, 118369.

[37] S. Verma, B. Kim, H.-R. M. Jhong, S. Ma, P. J. A. Kenis, *ChemSusChem* **2016**, *9*, 1972.

[38] T. T. H. Hoang, S. Ma, J. I. Gold, P. J. A. Kenis, A. A. Gewirth, *ACS Catal.* **2017**, *7*, 3313.

[39] T. Zhang, S. Verma, S. Kim, T. T. Fister, P. J. A. Kenis, A. A. Gewirth, *J. Electroanal. Chem.* **2020**, *875*, 113862.

[40] Y. Wang, H. Shen, K. J. T. Livi, D. Raciti, H. Zong, J. Gregg, M. Onadeko, A. Wan, A. Watson, C. Wang, *Nano Lett.* **2019**, *19*, 8461.

[41] D. Raciti, C. Wang, *ACS Energy Lett.* **2018**, *3*, 1545.

[42] D. Raciti, Y. Wang, J. H. Park, C. Wang, *ACS Appl. Energy Mater.* **2018**, *1*, 2392.

[43] S. Nitopi, E. Bertheussen, S. B. Scott, X. Liu, A. K. Engstfeld, S. Horch, B. Seger, I. E. L. Stephens, K. Chan, C. Hahn, J. K. Nørskov, T. F. Jaramillo, I. Chorkendorff, *Chem. Rev.* **2019**, *119*, 7610.

[44] Y. Gao, Q. Wu, X. Liang, Z. Wang, Z. Zheng, P. Wang, Y. Liu, Y. Dai, M.-H. Whangbo, B. Huang, *Adv. Sci.* **2020**, *7*, 1902820.

[45] Q. Lei, H. Zhu, K. Song, N. Wei, L. Liu, D. Zhang, J. Yin, X. Dong, K. Yao, N. Wang, X. Li, B. Davaasuren, J. Wang, Y. Han, *J. Am. Chem. Soc.* **2020**, *142*, 4213.

[46] Z. Chen, T. Wang, B. Liu, D. Cheng, C. Hu, G. Zhang, W. Zhu, H. Wang, Z.-J. Zhao, J. Gong, *J. Am. Chem. Soc.* **2020**, *142*, 6878.

[47] Y. C. Tan, K. B. Lee, H. Song, J. Oh, *Joule* **2020**, *4*, 1104.

[48] Z. Ma, C. Tsounis, P. V. Kumar, Z. Han, R. J. Wong, C. Y. Toe, S. Zhou, N. M. Bedford, L. Thomsen, Y. H. Ng, R. Amal, *Adv. Funct. Mater.* **2020**, *30*, 1910118.

[49] X. Chen, D. A. Henckel, U. O. Nwabara, Y. Li, A. I. Frenkel, T. T. Fister, P. J. A. Kenis, A. A. Gewirth, *ACS Catal.* **2020**, *10*, 672.

[50] M. Zhong, K. Tran, Y. Min, C. Wang, Z. Wang, C.-T. Dinh, P. De Luna, Z. Yu, A. S. Rasouli, P. Brodersen, S. Sun, O. Voznyy, C.-S. Tan, M. Askerka, F. Che, M. Liu, A. Seifitokaldani, Y. Pang, S.-C. Lo, A. Ip, Z. Ulissi, E. H. Sargent, *Nature* **2020**, *581*, 178.

[51] C. Hahn, T. Hatsukade, Y.-G. Kim, A. Vailionis, J. H. Baricuatro, D. C. Higgins, S. A. Nitopi, M. P. Soriaga, T. F. Jaramillo, *Proc. Natl. Acad. Sci. U. S. A.* **2017**, *114*, 5918.

[52] J.-J. Lv, M. Jouny, W. Luc, W. Zhu, J. J. Zhu, F. Jiao, *Adv. Mater.* **2018**, *30*, 1803111.

[53] S. Ma, R. Luo, M. Heima, M. Yamauchi, P. J. A. Kenis, *J. Power Sources* **2016**, *301*, 219.

[54] H. Yang, Y.-w. Hu, J.-j. Chen, M.-S. Balogun, P.-p. Fang, S. Zhang, J. Chen, Y. Tong, *Adv. Energy Mater.* **2019**, *9*, 1901396.

[55] K. P. Kuhl, T. Hatsukade, E. R. Cave, D. N. Abram, J. Kibsgaard, T. F. Jaramillo, *J. Am. Chem. Soc.* **2014**, *136*, 14107.

[56] H. A. Hansen, J. B. Varley, A. A. Peterson, J. K. Nørskov, *J. Phys. Chem. Lett.* **2013**, *4*, 388.

[57] F. Naseem, P. Lu, J. Zeng, Z. Lu, Y. H. Ng, H. Zhao, Y. Du, Z. Yin, *ACS Nano* **2020**, *14*, 7734.

[58] L. Wang, W. Chen, D. Zhang, Y. Du, R. Amal, S. Qiao, J. Wu, Z. Yin, *Chem. Soc. Rev.* **2019**, *48*, 5310.

[59] S. Ma, M. Sadakiyo, M. Heima, R. Luo, R. T. Haasch, J. I. Gold, M. Yamauchi, P. J. A. Kenis, *J. Am. Chem. Soc.* **2017**, *139*, 47.

[60] D. Chen, Y. Wang, D. Liu, H. Liu, C. Qian, H. He, J. Yang, *Carbon Energy* **2020**, *2*, 443.

[61] T. T. H. Hoang, S. Verma, S. Ma, T. T. Fister, J. Timoshenko, A. I. Frenkel, P. J. A. Kenis, A. A. Gewirth, *J. Am. Chem. Soc.* **2018**, *140*, 5791.

[62] X. Zhang, S. Han, B. Zhu, G. Zhang, X. Li, Y. Gao, Z. Wu, B. Yang, Y. Liu, W. Baaziz, O. Ersen, M. Gu, J. T. Miller, W. Liu, *Nat. Catal.* **2020**, *3*, 411.

[63] W. Zhanga, C. Xua, Y. Hua, S. Yang, L. Ma, L. Wang, P. Zhao, C. Wang, J. Ma, Z. Jin, *Nano Energy* **2020**, *73*, 104796.

[64] Y.-T. Pan, H. Yang, *Nano Today* **2020**, *31*, 100832.

[65] E. L. Clark, C. Hahn, T. F. Jaramillo, A. T. Bell, *J. Am. Chem. Soc.* **2017**, *139*, 15848.

[66] J. Huang, M. Mensi, E. Oveisi, V. Mantella, R. Buonsanti, *J. Am. Chem. Soc.* **2019**, *141*, 2490.

[67] Z. Chang, S. Huo, W. Zhang, J. Fang, H. Wang, *J. Phys. Chem. C* **2017**, *121*, 11368.

[68] J. Gao, H. Zhang, X. Guo, J. Luo, S. M. Zakeeruddin, D. Ren, M. Grätzel, *J. Am. Chem. Soc.* **2019**, *141*, 18704.

[69] X. Lv, L. Shang, S. Zhou, S. Li, Y. Wang, Z. Wang, T.-K. Sham, C. Peng, G. Zheng, *Adv. Energy Mater.* **2020**, *10*, 2001987.

[70] L. Hou, J. Han, C. Wang, Y. Zhang, Y. Wang, Z. Bai, Y. Gu, Y. Gao, X. Yan, *Inorg. Chem. Front.* **2020**, *7*, 2097.

[71] G. A. Kamat, C. Yan, W. T. Osowiecki, I. A. Moreno-Hernandez, M. Ledendecker, A. P. Alivisatos, *J. Phys. Chem. Lett.* **2020**, *11*, 5318.

[72] W. T. Osowiecki, X. Ye, P. Satish, K. C. Bustillo, E. L. Clark, A. P. Alivisatos, *J. Am. Chem. Soc.* **2018**, *140*, 8569.

[73] T. Ngo, H. Yang, *J. Phys. Chem. Lett.* **2015**, *6*, 5051.

[74] J. Wu, M. Shi, X. Yin, H. Yang, *ChemSusChem* **2013**, *6*, 1888.

[75] X. Yin, M. Shi, J. Wu, Y.-T. Pan, D. L. Gray, J. A. Bertke, H. Yang, *Nano Lett.* **2017**, *17*, 6146.

[76] M. Shi, H. S. Kwon, Z. Peng, A. Elder, H. Yang, *ACS Nano* **2012**, *6*, 2157.

[77] W. Zhou, J. Wu, H. Yang, *Nano Lett.* **2013**, *13*, 2870.

[78] J. Wu, Y.-T. Pan, D. Su, H. Yang, *Sci. China Mater.* **2015**, *58*, 595.

[79] A. Khorshidi, J. Violet, J. Hashemi, A. A. Peterson, *Nat. Catal.* **2018**, *1*, 263.

[80] M. Karamad, H. A. Hansen, J. Rossmeisl, J. K. Nørskov, *ACS Catal.* **2015**, *5*, 4075.

[81] A. G. M. da Silva, T. S. Rodrigues, S. J. Haigh, P. H. C. Camargo, *Chem. Commun.* **2017**, *53*, 7135.

[82] C. M. Cobley, Y. Xia, *Mater. Sci. Eng., R* **2010**, *70*, 44.

[83] D. Li, C. Wang, D. Tripkovic, S. Sun, N. M. Markovic, V. R. Stamenkovic, *ACS Catal.* **2012**, *2*, 1358.

[84] J. Wu, H. Yang, *Nano Res.* **2011**, *4*, 72.

[85] S. Verma, X. Lu, S. Ma, R. I. Masel, P. J. A. Kenis, *Phys. Chem. Chem. Phys.* **2016**, *18*, 7075.